Developmental HCN channelopathy results in decreased neural progenitor proliferation and microcephaly in mice

Anna Katharina Schlusche[a,b,1], Sabine Ulrike Vay[c], Niklas Kleinenkuhnen[c], Steffi Sandke[d,2], Rafael Campos-Martín[c], Marta Florio[e,3], Wieland Huttner[e], Achim Tresch[c,f], Jochen Roeper[g], Maria Adele Rueger[c,h], Igor Jakovcevski[a,b,h], Malte Stockebrand[a,b,4], and Dirk Isbrandt[a,b,h,4,5]

[a]German Center for Neurodegenerative Diseases, 53175 Bonn, Germany; [b]Institute for Molecular and Behavioral Neuroscience, Faculty of Medicine and University Hospital Cologne, University of Cologne, 50937 Cologne, Germany; [c]Faculty of Medicine, University Hospital Cologne, University of Cologne, 50937 Cologne, Germany; [d]Center for Molecular Neurobiology, University Hamburg, 20246 Hamburg, Germany; [e]Max Planck Institute of Molecular Cell Biology and Genetics, 01307 Dresden, Germany; [f]Center for Data and Simulation Science, University of Cologne, 50937 Cologne, Germany; [g]Institute of Neurophysiology, Goethe University Frankfurt, 60590 Frankfurt, Germany; and [h]Center for Molecular Medicine Cologne, University of Cologne, 50937 Cologne, Germany

Edited by Lily Yeh Jan, HHMI, University of California, San Francisco, CA, and approved July 7, 2021 (received for review May 11, 2020)

The development of the cerebral cortex relies on the controlled division of neural stem and progenitor cells. The requirement for precise spatiotemporal control of proliferation and cell fate places a high demand on the cell division machinery, and defective cell division can cause microcephaly and other brain malformations. Cell-extrinsic and -intrinsic factors govern the capacity of cortical progenitors to produce large numbers of neurons and glia within a short developmental time window. In particular, ion channels shape the intrinsic biophysical properties of precursor cells and neurons and control their membrane potential throughout the cell cycle. We found that hyperpolarization-activated cyclic nucleotide-gated cation (HCN) channel subunits are expressed in mouse, rat, and human neural progenitors. Loss of HCN channel function in rat neural stem cells impaired their proliferation by affecting the cell-cycle progression, causing G1 accumulation and dysregulation of genes associated with human microcephaly. Transgene-mediated, dominant-negative loss of HCN channel function in the embryonic mouse telencephalon resulted in pronounced microcephaly. Together, our findings suggest a role for HCN channel subunits as a part of a general mechanism influencing cortical development in mammals.

HCN channelopathy | brain development | microcephaly | cell cycle

Cell proliferation is a tightly regulated process consisting of multifaceted and complex control mechanisms. Defective cell cycle checkpoints, or the dysfunction of cell cycle regulators, affect the physiological or pathological fate of stem and neural progenitor cells (NPCs), and defects in these processes can cause microcephaly and other brain malformations (1). While the molecular and biochemical mechanisms of cell cycle control are well established, the bioelectrical modulation of cell cycle progression by ion channels is still poorly understood. Ion channel activity has been suggested to regulate proliferation through its effect on the membrane potential. Notably, it had been shown that nonproliferative cells had lower resting membrane potential than proliferative cells and that the membrane potential changed during cell cycle progression (2, 3). The hyperpolarization of dividing tumor cells induced cell cycle arrest (2), while the strong depolarization of even postmitotic neurons induced their proliferation (4, 5). Furthermore, a recent study showed that the resting membrane potential of mouse cortical progenitors influenced their neurogenic differentiation (6). During development, the profile of ion channels expressed by progenitor cells exhibits changes and so do the biophysical properties they are endowed with (7–9). In particular, K^+ channels, such as the *ether-a-go-go* gene family members EAG and ERG, have been linked to cell cycle progression due to their cell cycle phase-specific expression and function (for review, refer to ref. 3). Together, the data, which were predominantly obtained from cultured and tumor cell lines, suggest a close relationship between membrane potential and the well-investigated cyclin-dependent pathways. The altered function of ion channels that contribute to the control of the membrane potential in neural stem and progenitor cells could, therefore, affect proliferation or differentiation and impair brain development.

Recently, several patients with early infantile epileptic encephalopathy (EIEE) were reported to have mutations in *HCN1*, which encodes a pore-forming subunit of hyperpolarization-activated cyclic nucleotide-gated cation (HCN) channels (10, 11). Two unrelated patients carried the *HCN1* missense loss-of-function mutation p.M305L and presented with epilepsy and a deceleration of

Significance

Impaired cell cycle regulation of neural stem and progenitor cells can affect cortical development and cause microcephaly. During cell cycle progression, the cellular membrane potential changes through ion channel activity and tends to be more depolarized in proliferating cells. Hyperpolarization-activated cyclic nucleotide-gated cation (HCN) channels, which mediate a depolarizing current in neurons and cardiac cells, are linked to neurodevelopmental diseases and also contribute to the control of cell cycle progression and proliferation of neuronal precursor cells. In this study, HCN channel deficiency during embryonic brain development resulted in marked microcephaly of mice with impaired HCN channel function in dorsal forebrain progenitors. The findings suggest that HCN channel subunits are part of a general mechanism influencing cortical development in mammals.

Author contributions: A.K.S., M.S., and D.I. designed research; A.K.S., S.U.V., S.S., J.R., I.J., and M.S. performed research; A.K.S., S.U.V., N.K., R.C.-M., M.F., A.T., J.R., I.J., and M.S. analyzed data; A.K.S., S.U.V., W.H., M.A.R., M.S., and D.I. wrote the paper; and A.T. and I.J. edited the paper.

The authors declare no competing interest.

This article is a PNAS Direct Submission.

[1]Present address: Center for Neurogenetics, Brain and Mind Research Institute, Weill Cornell Medicine, New York, NY 10021.

[2]Present address: Department of Internal Medicine III, University Hospital Heidelberg, 69120 Heidelberg, Germany.

[3]Present address: Department of Genetics, Harvard Medical School, Boston, MA 02115.

[4]M.S. and D.I. contributed equally to this work.

[5]To whom correspondence may be addressed. Email: dirk.isbrandt@dzne.de.

This article contains supporting information online at https://www.pnas.org/lookup/suppl/doi:10.1073/pnas.2009393118/-/DCSupplemental.

Published August 24, 2021.

head growth resulting in microcephaly (10). In the absence of overt signs of structural changes in these patients, such as altered gyration, focal dysplasia, or enlarged subarachnoidal space or ventricles in cerebral magnetic resonance tomography, we sought to investigate whether *HCN* channelopathies might affect processes of brain development that could impair brain growth. Mutations in *HCN1* are associated with a broad spectrum of developmental disorders, including intellectual disability and autism spectrum disorder, atypical Rett syndrome with microcephaly (11), generalized epilepsy, febrile seizures plus spectrum, and EIEE (10, 12). Moreover, HCN channel dysfunction can also be acquired following experimental febrile seizures (13, 14), or in chronic epilepsy (15), affecting, for example, the epigenetic regulation through neurogenesis repressor element 1 (RE1)-silencing transcription factor (REST)/neuron-restrictive silencer factor (NRSF) (16).

While the contribution of HCN channels to biophysical properties of adult neurons is well established (17), their roles in brain development are mostly unknown. During postnatal rodent brain development, HCN channels undergo substantial and subunit-specific developmental regulation (7, 18–20). The four different pore-forming alpha subunits (HCN1 to HCN4) assemble into homo- or heteromeric tetramers (17). HCN channels are active at subthreshold membrane potentials and mediate I_h, a voltage-dependent cation current activated by membrane hyperpolarization, which, in turn, depolarizes the membrane potential toward the action potential threshold and, thus, contributes to the dynamic control of the resting membrane potential and subthreshold integration (17). When active in stem cells, HCN channels could contribute to membrane depolarization or membrane voltage oscillations throughout the cell cycle. As the pharmacological inhibition of HCN channels in cultured embryonic stem cells affected proliferation and differentiation (21, 22), neural stem and progenitor cells could similarly be affected by the impaired function of HCN channels (23).

In this study, we sought to address whether the loss of HCN channel function would affect brain development. Using transgenic mouse lines with altered HCN channel activity in the embryonic telencephalon and pharmacological inhibition of I_h in cultured embryonic rat cortical neural stem cells (NSCs), we show that the loss of HCN channel function impaired cell cycle progression and proliferation and caused a pronounced microcephaly phenotype. We, thus, propose a mechanistic link between *HCN* channel dysfunction and microcephaly in mice that may contribute to pathological cortical development in patients with *HCN* channelopathies.

Results

Expression of HCN Subunits during Brain Development. The four HCN subunits, HCN1 to HCN4, are expressed at various levels in the mammalian central nervous system and are known to form homomeric or heteromeric channels (17, 24). In the rat hippocampus, expression of the HCN1, 2, and 4 subunits changes during postnatal development. HCN1 and HCN2 are increasing, while HCN4 is decreasing with maturation (7, 18, 19). Therefore, we first determined the subunit-specific spatiotemporal expression patterns of HCN1 to HCN4 in the mammalian forebrain, focusing on embryonic development. An analysis of messenger RNA (mRNA) levels throughout pre- and postnatal mouse forebrain development revealed a monotonically increasing expression of *Hcn1* and *Hcn2*, whereas *Hcn3* and *Hcn4* expression levels peaked at embryonic day (E) 15 followed by a decrease (Fig. 1*A* and *SI Appendix*, Fig. S1 *A–C* and *A'–C'*). *Hcn3* was the most abundantly expressed subunit at E13 to E18. *Hcn4* was the second highest expressed *Hcn* transcript at E13 that was present at levels comparable to that seen in *Hcn1* and *Hcn2* at E15 to E18, after which it declined. Immunoblots of E15 mouse embryonic brain lysates revealed HCN3 and HCN4 subunit proteins, while those of HCN1 and HCN2 were below the detection limits of the antibodies used (Fig. 1*B*). Prenatal expression of the HCN subunits in the developing human brain investigated by exon array hybridization of complementary DNAs (cDNAs) generated from the total RNA of frozen tissue samples (25) was detected during the earliest analyzed time period of late embryonic development (4 to 8 wk post-conception). As in developing mouse brain, *HCN3* and *HCN4* peaked during early to mid-fetal periods. Except for the thalamus, all brain regions showed a similar time course of expression (*SI Appendix*, Fig. S2). *HCN1* and *HCN2* increased at mid-gestation and reached almost adult-like levels around birth and during the first year of life (*SI Appendix*, Fig. S2).

Transcriptome analyses of select neural progenitor subpopulations and of young neurons isolated from E14.5 embryonic mouse and human fetal neocortex at 13 wk post-conception (26) indicated that *HCN3* was the main HCN subunit detected in both species (*SI Appendix*, Fig. S1 *D* and *E*).

At single-cell resolution, the transcriptome analysis of the developing brains from E9 to E13 mouse embryos [data set III (27)] revealed the presence of *Hcn1*, *Hcn3*, and *Hcn4* transcripts in different classes of progenitors (*SI Appendix*, Fig. S1 *F* and *G*). Although at low levels, HCN subunits were detected in the cell cluster expressing early stem cell/apical radial glia cell markers (Pax6, Sox2, Mki67) in the apical radial glia-specific marker- (Eomes/Tbr2, Neurog2) expressing cell cluster and in the cell cluster expressing the neuronal marker Tubb3 (TuJ1) (*SI Appendix*, Fig. S1 *F–H*). In 5% of late progenitors/immature neurons (NPC), any of the HCN subunits were detectable, with *Hcn4* and *Hcn3* being the most prevalent subunits, which was also true of oligodendrocyte progenitor cells (OPC). While 3% of NSCs expressed HCN subunits, most prominently *Hcn1*, *Hcn3*, and *Hcn4* (*SI Appendix*, Fig. S1*G*). Interestingly, Cajal–Retzius cells showed the highest expression of *Hcn* transcripts (*SI Appendix*, Fig. S1*G*).

Single-cell RNA sequencing (scRNA-seq) of primary cultured embryonic E14.5 rat cortical NSCs using two different technical platforms revealed the presence of *Hcn1-4* in about 8% of NSCs analyzed using the well-based counts (WaferGen platform) and of *Hcn3* and *Hcn4* in 2.4% of the cells using the drop-seq. (10X Genomics platform) expression results (*SI Appendix*, Fig. S3 *A* and *B*). In line with these findings, immunoreactivity against HCN3 was most frequently detected in rat NSCs (12.2 ± 0.8% of cells) followed by HCN4 (9.2 ± 1.3%) (*SI Appendix*, Fig. S3*C*), which was also detected in cortical sections from E13 embryos (*SI Appendix*, Fig. S1*I*), and HCN1 (6.2 ± 2.2%) (*SI Appendix*, Fig. S3*C*). Using the patch clamp technique, we detected I_h-like currents in only a small subset of cultured NSCs (*SI Appendix*, Fig. S3*D*), which, together with the mRNA expression data, suggests the presence of a heterogeneous cell population or only a short-lived presence of HCN channels in the cell membrane. Together, these results provide evidence for the embryonic expression of HCN subunits and indicate a potential role for HCN1, HCN3, and HCN4 subunits in the developing telencephalon. As HCN subunits assemble into homo- or heteromeric tetramers (17), the presence of several HCN subtypes suggested that pharmacological or genetic dominant-negative strategies targeting HCN channel function in a subunit-independent manner were most likely to unmask a role for I_h in embryonic brain development. In contrast to previous mouse models with single HCN subunit knockouts (28–31), we generated conditional transgenic Tet-Off mouse lines expressing the hHCN4(p.Gly480Ser) subunit (HCN-DN) and an eGFP reporter in mouse forebrain (Fig. 1*C*).

Loss of HCN Channel Function in Forebrain NPCs Causes Microcephaly. Expression of HCN-DN was designed to ablate I_h by the formation of nonconducting heteromeric channels with the endogenous HCN1-4 subunits (*SI Appendix*, Fig. S4), which was prevented by the addition of doxycycline to the animals' drinking water or chow (Fig. 1 *C* and *E*). This dominant-negative strategy was previously used by us to study HCN or Kv7 channel function in the heart (32) or brain (33, 34), respectively. In adult mouse hippocampal CA1 pyramidal neurons (targeted by utilizing the CaMKII promoter)

(Fig. 1*C*), which predominantly express HCN1 and HCN2 subunits, the presence of HCN-DN led to a robust and doxycycline-dependent ablation of I_h (Fig. 1 *D* and *E*). Embryonic expression of HCN-DN was achieved under the control of the EMX1 promoter (EMX1-HCN-DN mutants), which started expression confined to the dorsal telencephalon at approximately E9.5 (Fig. 1*F*). On

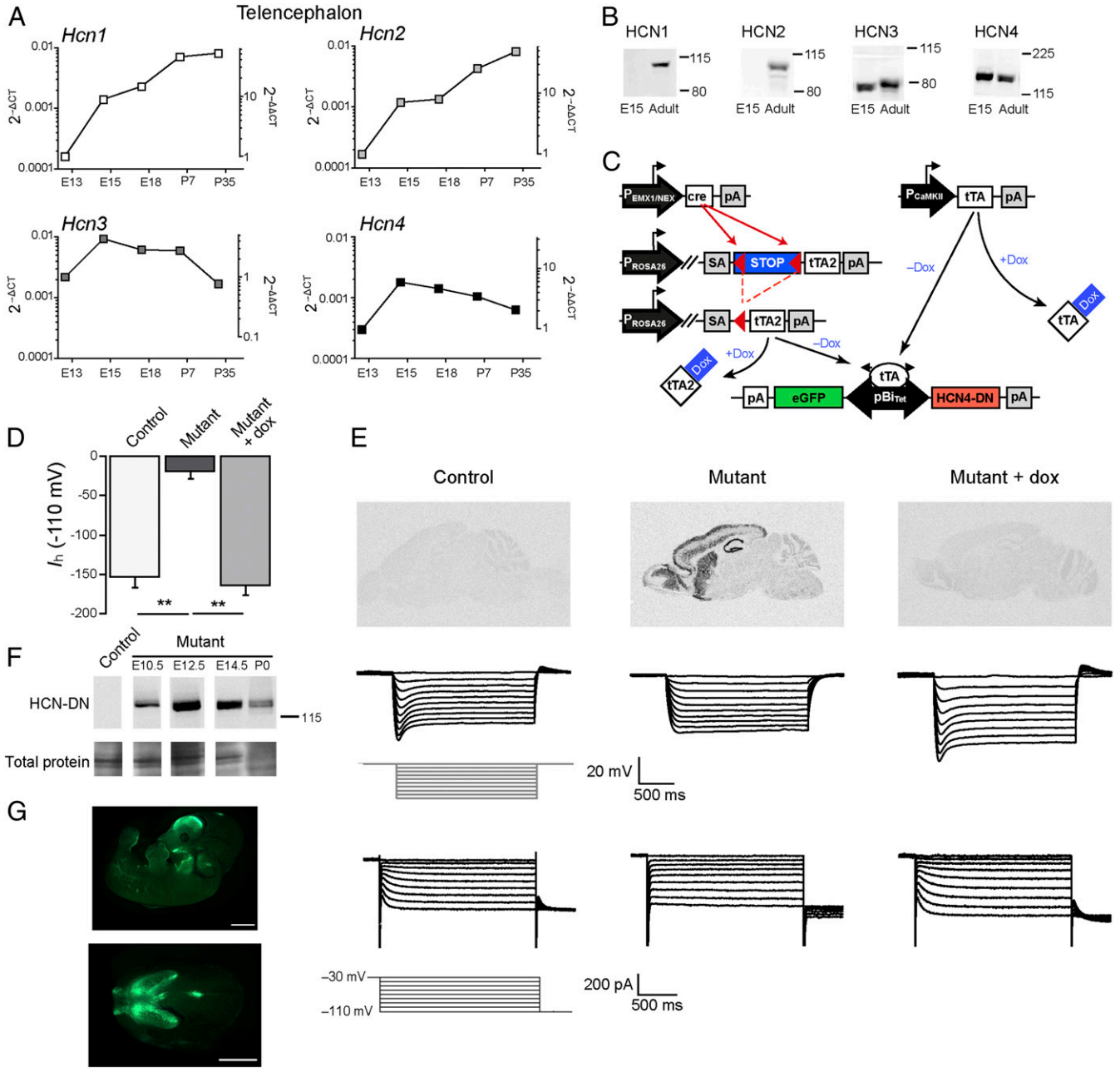

Fig. 1. Embryonic HCN subunit expression in mouse forebrain and dominant-negative transgenic strategy. (*A*) qRT-PCR analysis of *Hcn1-Hcn4* mRNA expression levels in mouse forebrain normalized to GAPDH mRNA ($2^{-\Delta CT}$, Left *y*-axis) and GAPDH and of the respective HCN subunit expression level at E13 ($2^{-\Delta\Delta CT}$, Right *y*-axis). (*B*) Immunoblot analysis of total brain lysates with HCN subtype-specific antibodies at embryonic day E15 and at the adult age. (*C*) Schematic overview of the mouse lines expressing the dominant-negative HCN4 subunit (HCN-DN) in embryonic or adult mouse brains. The embryonic expression was controlled by the EMX1 or NEX promoters driving Cre-recombinase expression, which removed the floxed stop cassette preceding the tetracycline transactivator (tTA2). Postnatal expression of HCN-DN was driven by the CaMKII promoter. In the absence of doxycycline, HCN-DN, which has an N-terminal hemagglutinin (HA) tag, and eGFP were expressed from the bidirectional tetracycline-responsive promoter pBi_{Tet}. (*D*) Summary statistics from voltage clamp experiments shown in *E* revealed markedly reduced I_h amplitudes in HCN-DN–expressing mutant cells (**$P < 0.01$; one-way ANOVA with Tukey's post hoc test). (*E*) Doxycycline and genotype-dependent transgene expression in the brain was tested in in situ hybridization experiments using HCN-DN–specific probes (*Top*). The traces are representative of current clamp (*Middle*) or voltage clamp recordings (*Bottom*) from CA1 pyramidal neurons in acute slice preparations from adult control ($n = 14$ cells; 4 mice), mutant ($n = 11$ cells; 4 mice), and doxycycline (dox)-treated mutant (mutant + dox, $n = 9$ cells; 2 mice) CaMKIIα-HCN-DN mice. The protocols are shown below the control traces. (*F*) Immunoblot detection of the HA-tag of the HCN-DN transgene in tissue lysates from mutant EMX1-HCN-DN brains at E10.5, 12.5, 14.5, at P0, and at E10.5 in a control brain. (*G*) eGFP expression in the whole embryo and head of E12.5 EMX1-HCN-DN mutants. (Scale bars, 1 mm.) Data are presented as mean ± SEM; Experiments in *A*, *B*, and *F* represent individual examples. Images in *G* are representative of five animals.

embryonic day 12.5 (E12.5), postnatal day 0 (P0), and P21, eGFP expression was mainly restricted to the telencephalon (Figs. 1*G* and 2*A*), with the exception of a small region in the mesencepahlic vesicle and partial skin expression (Fig. 1*G*). The visible expression outside of the nervous system is in agreement with the known EMX1 expression (35). Control littermates, which lacked at least one of the three alleles comprising a functional Tet-Off system (Fig. 1*C*), did not differ with respect to body weights, brain volumes, and relative ventricle volumes (*SI Appendix*, Fig. S5). Triple-transgenic EMX1-HCN-DN mutants were viable but showed a decrease in body weight at birth (P0), which was even more pronounced at P21 (Fig. 2 *B* and *C*) and likely to be caused by developmental delay and reduced fitness as compared to their control littermates. At both time points, the forebrain morphology was severely altered, including a marked reduction in the cortex size and the absence of hippocampal pyramidal layers (Fig. 2 *D* and *E*). Using magnetic resonance volumetry, we quantified brain and ventricle volumes at P0 and P21. We found a marked reduction in brain volume at both ages and an increase in ventricle volume at P21 (Fig. 2 *G*–*J*). The restriction of HCN-DN expression to postnatal development by the application of doxycycline until P0 prevented the changes in body weight and the development of a microcephalic phenotype (Fig. 2), ruling out a postnatal or a positional effect of the transgene.

Early Embryonic Ablation of HCN or I_h Inhibition in Neural Stem Cells Leads to Decreased Proliferation Because of Cell Cycle Arrest in G1 Phase. To analyze the mechanism underlying the marked microcephaly, we sought to investigate the critical processes of embryonic brain development that could impact brain size, such as neural progenitor cell proliferation, neuronal differentiation, apoptosis, and migration. At E12.5, most of the cells in the control or EMX1-HCN-DN cortex were Pax6-expressing radial glia cells (Fig. 3*A*). As early as at this stage, a markedly reduced thickness of the mutant cortex was evident and accompanied by an increase in the apoptosis marker cleaved Caspase-3 and a decrease in the proliferation marker Ki67 (Fig. 3 *B*–*E*). The latter was not restricted to embryonic stages but similarly found at P0, when the number of Ki67-immunoreactive cells in the ventricular and subventricular zones (VZ/SVZ) was reduced (Fig. 3 *F* and *G*). No increase was found in apoptotic cells at P0, however (SI Appendix, Fig. S6 *A* and *B*). A comparable number of proliferative cells was found in the sensorimotor cortex that likely reflected the ongoing gliogenesis in newborn mice (Fig. 3 *F*–*H*). To test whether the microcephaly phenotype was linked to the loss of HCN channel function and not to an artifact of the HCN-DN and eGFP transgenes, we used the same EMX1 promoter line as in EMX1-HCN-DN mice to coexpress eGFP and a cAMP-insensitive HCN4 channel subunit (HCN4-573X), which, in contrast to HCN-DN subunits, does form functional channels (36). The resulting EMX1-HCN4-573X mice did not show structural changes (*SI Appendix*, Fig. S7) when analyzed at the age of 15 wk.

We next generated mice in which HCN-DN expression was initiated in Nex (*Neurod6*)-expressing cells using the NEX-cre promoter line (NEX-HCN-DN mutants), which initiates cre-dependent gene expression starting at E10.5 in the SVZ, intermediate zone, and cortical plate (37, 38). Unexpectedly, the brain morphology of NEX-HCN-DN mice was equally unaffected (*SI Appendix*, Fig. S8) as in EMX1-HCN4-573X mice. This result prompted us to characterize *Emx1* and Nex/*Neurod6* expression in the mouse embryonic scRNA-seq dataset (27) in more detail. In contrast to *Emx1*, Nex/*Neurod6* expression was virtually absent from the NSC cell cluster and, only to a minor extent, overlapped with the expression of *Mki67* (*SI Appendix*, Fig. S9 *F* and *G*). These expression data indicate predominant Nex/*Neurod6* expression in nonproliferating cells in the developing brains of E9 to E13 embryos, which is in line with previous findings that cre-positive cells in NEX-cre mice did not incorporate bromodeoxyuridine (BrdU) at E16 (38). These results indicate that microcephaly in EMX1-HCN-DN mice is linked to the loss of HCN channel function in NSCs of the VZ, thereby supporting the notion that functional HCN channels are needed for proper cell cycle progression in NSCs.

To further test our hypothesis, we employed a different experimental system and analyzed the early developmental processes in NSCs from E13.5 rat cortices using the pharmacological I_h inhibitor ZD7288. Both the quantification of the mRNA levels of the proliferating cell marker Ki67 and percentage of BrdU-incorporating cells (cells in S phase) showed a ZD7288 dose-dependent decrease in proliferation (Fig. 3 *I* and *J*). Transcriptome analysis of scRNA-seq experiments of cultured NSCs displayed a clear separation between control and ZD7288-treated cell clusters (Fig. 3*K*). To link transcriptomic data to biological pathways, we performed enrichment analysis of differentially regulated Kyoto Encyclopedia of Genes and Genomes (KEGG) pathways, revealing DNA replication and cell cycle as the two most affected pathways (Table 1). The determination of the cell cycle phases showed that the majority of ZD7288-treated NSCs (82.8%) were in G1 as compared to control cells (7.0%), which were predominantly in the S and G2/M phases (Fig. 3 *K*, *Inset*). After regressing out the variance explainable by the cell cycle marker genes from the dataset, the cells did no longer form clusters specific to their treatment (Fig. 3*L*). The complementary, drop-seq–based NSC scRNA-seq dataset II, which had higher cell numbers at the expense of visual single-cell shape control and sequencing depth, confirmed, although to a lower extent, G1 accumulation after pharmacological I_h inhibition (*SI Appendix*, Fig. S10). These results suggest the mechanism underlying the decrease in NSC proliferation is likely to be an I_h inhibition-induced increase in the length of the G1 cell cycle phase that severely affects cell cycle progression.

In both datasets, HCN subunit-expressing untreated or ZD7288-treated NSCs did not cluster in clearly identifiable subclusters or cell types and, thus, did not contribute to the identification of a specific progenitor type (*SI Appendix*, Fig. S10 *B* and *E*). The increased cell numbers allowed cell cycle phase-specific differential gene expression analysis to be performed and revealed differential regulation of genes involved in cell cycle progression, associated with microcephaly, cortical neurogenesis, and stem cell differentiation (*Asns*, *Psat1*) (*SI Appendix*, Table S1) (39–41). Of note, we found a substantial overlap of differentially regulated genes after I_h inhibition in the rat NSC culture with an early developmental transcriptomic signature in cortical extracts from the Elp3 conditional knockout (Elp3cKO) microcephaly mouse model with impaired indirect neurogenesis because of endoplasmic reticulum (ER) stress and unfolded protein response (UPR) (42). In comparison, 13 out of 82 and 45 out of 405 differentially regulated genes in dataset I and in dataset II, respectively, were also differentially regulated in the Elp3cKO mice (Dataset S1).

Effects of Genetic or Pharmacological I_h Inhibition on Differentiation, Migration, and Cell Death. Next, we investigated the levels of the glial proteins glial fibrillary acidic protein (GFAP) and 2′,3′-cyclic-nucleotide 3′-phosphodiesterase (CNPase) and the neuron-specific TuJ1 as markers of differentiation in brains from EMX1-HCN-DN mice and in cultured neural progenitors after a ZD7288-mediated block of I_h. In P0 mouse brains, we found higher immunoreactivity levels for GFAP (astrocytes) and CNPase (oligodendrocytes) in EMX1-HCN-DN mutants compared to those in control littermates but no difference in TuJ1 levels (Fig. 4 *A*–*D*). In cultured primary rat NSCs, differentiation was initiated by FGF2 withdrawal, which induced a comparable decrease in the ratio of Sox2-positive cells in vehicle- or ZD7288-treated cells over time (Fig. 4*E*). While the proportion of cells expressing the marker for both immature and mature neurons TuJ1 was decreased by ZD7288 5 d after FGF2 withdrawal (Fig. 4*F*), the ratios of the markers for astrocytes (GFAP) and oligodendrocytes (CNPase) were not significantly altered upon I_h inhibition (Fig. 4 *G* and *H*). Furthermore, neither HCN-DN expression in neural precursors induced at E15 by in

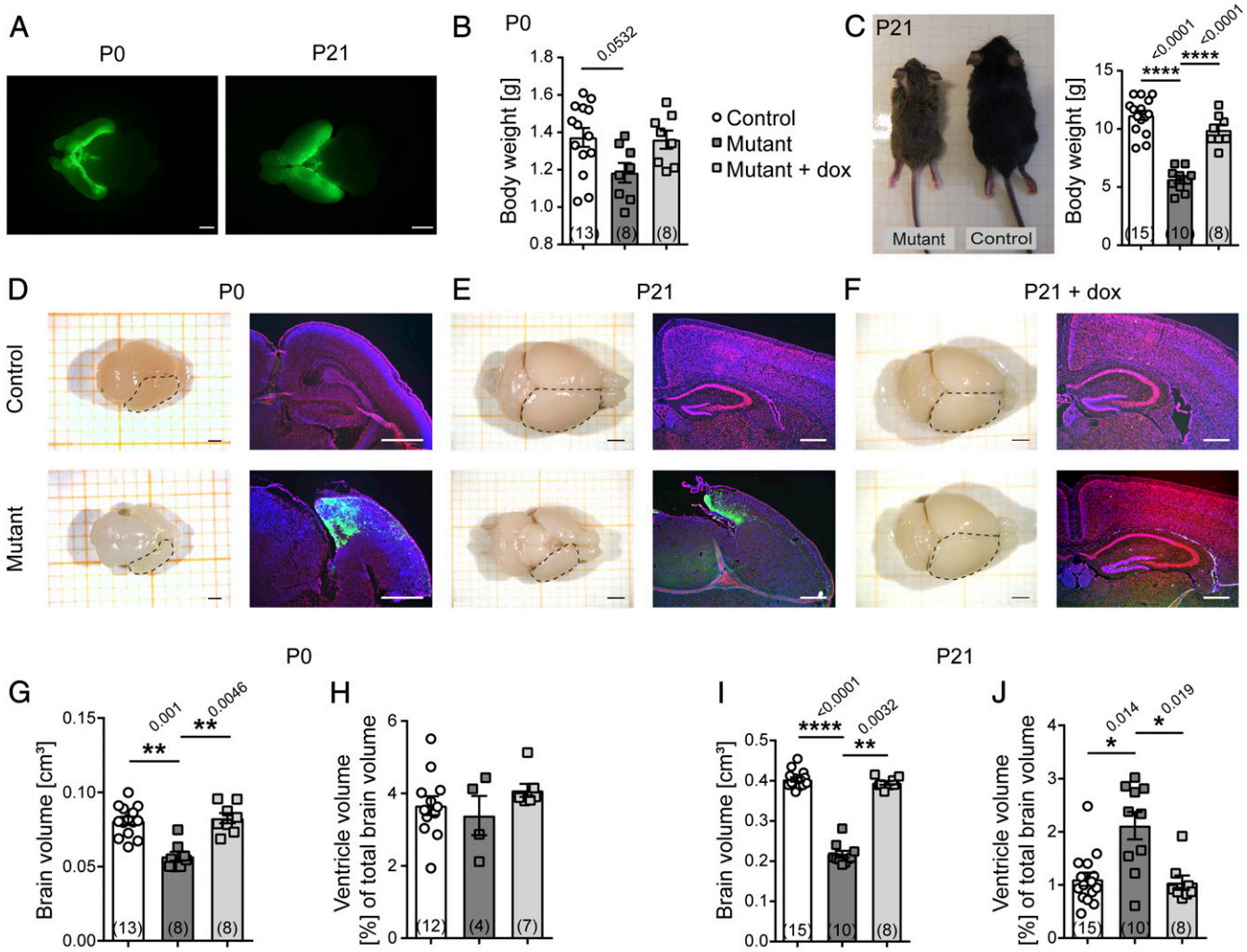

Fig. 2. Development-dependent structural changes in I_h-deficient mice. (*A*) eGFP expression in P0 and P21 EMX1-HCN-DN mouse brains is restricted to the forebrain. Body weights of (*B*) P0 and (*C*) P21 EMX1-HCN-DN mutant mice were lower than those of control animals and mutants on doxycycline until P0 (mutant + dox) (one-way ANOVA with Tukey's post hoc test). Macroscopic top views of explanted brains and fluorescent Nissl staining (red) of coronal brain slices of EMX1-HCN-DN mice at (*D*) P0, (*E*) P21, and of (*F*) P21 mutant + dox. Slices were counterstained with DAPI (blue), and eGFP is depicted in green. (*G*) Absolute brain volumes and (*H*) ventricle volumes as a fraction of the total brain volume of P0 EMX1-HCN-DN mice compared to those of control and mutant + dox animals. (*I*) Absolute brain volumes and (*J*) ventricle volumes as a fraction of total brain volume of P21 EMX1-HCN-DN compared to those of mutant + dox and control mice. (Kruskal–Wallis with post hoc Dunn's test.) (Scale bars in P0 brains in *A* and *D*, 1 mm, in P21 brains in *A*, *E*, and *F*, 2 mm, in sections, 500 μm.) Data are presented as mean ± SEM; *n* is given in parentheses; *P* values are above asterisks. Images in *D–F*, *Right* are representative of one experiment, and in *A* and *D–F*, *Left* corresponding to *n* in *G–J*.

utero electroporation nor the ZD7288-mediated block of I_h in cultured NSCs affected cell migration (*SI Appendix*, Fig. S6 *E–G*). Unlike in sections from the E12.5 embryonic cortex (Fig. 3 *B* and *D*), we did not find evidence for increased apoptosis/necrosis in the rat NSC cultures treated with ZD7288 (*SI Appendix*, Fig. S6 *C* and *D*). Likewise, Ca^{2+} handling of NSCs was not altered in a systematic way after application of ZD7288 (*SI Appendix*, Fig. S6 *H* and *I*).

Discussion

Together, our findings establish a hitherto unknown role for HCN channels in the proliferation of neural stem and progenitor cells by affecting cell cycle progression and the exit from the G1 cell cycle phase. The pharmacological approach, in combination with the genetic ablation of I_h, suggests an ionic current-dependent mechanism underlying this phenotype. This notion is further supported by the analysis of the EMX1-HCN4-573X mouse line, which expressed a cAMP-insensitive, but otherwise functional, HCN4 subunit in the embryonic telencephalon and did not show morphological alterations of the forebrain structure (*SI Appendix*, Fig. S7). Likewise, NEX-HCN-DN mutants in which cre-dependent transgene expression starts only about 1 d later than in EMX1-cre mice in the SVZ, intermediate zone, and cortical plate (37, 38) displayed normal brain morphology. Unlike *Emx1* expression, Nex/*Neurod6* expression was virtually absent from the NSC and proliferating cell clusters, indicating that Nex/*Neurod6* was predominantly expressed in non-proliferating cells in the developing brains of E9 to E13 mouse embryos (*SI Appendix*, Fig. S9 *F* and *G*). The results obtained using these complementary genetic strategies provide evidence that the marked microcephaly was caused by the loss of HCN channel function in NSCs of the VZ rather than by off-target effects of the transgenic approach, thereby supporting the notion that functional HCN channels are needed for proper cell cycle progression in NSCs.

Although we and others (23) did not find marked ZD7288-induced changes in the differentiation of cultured NSCs, in addition to the

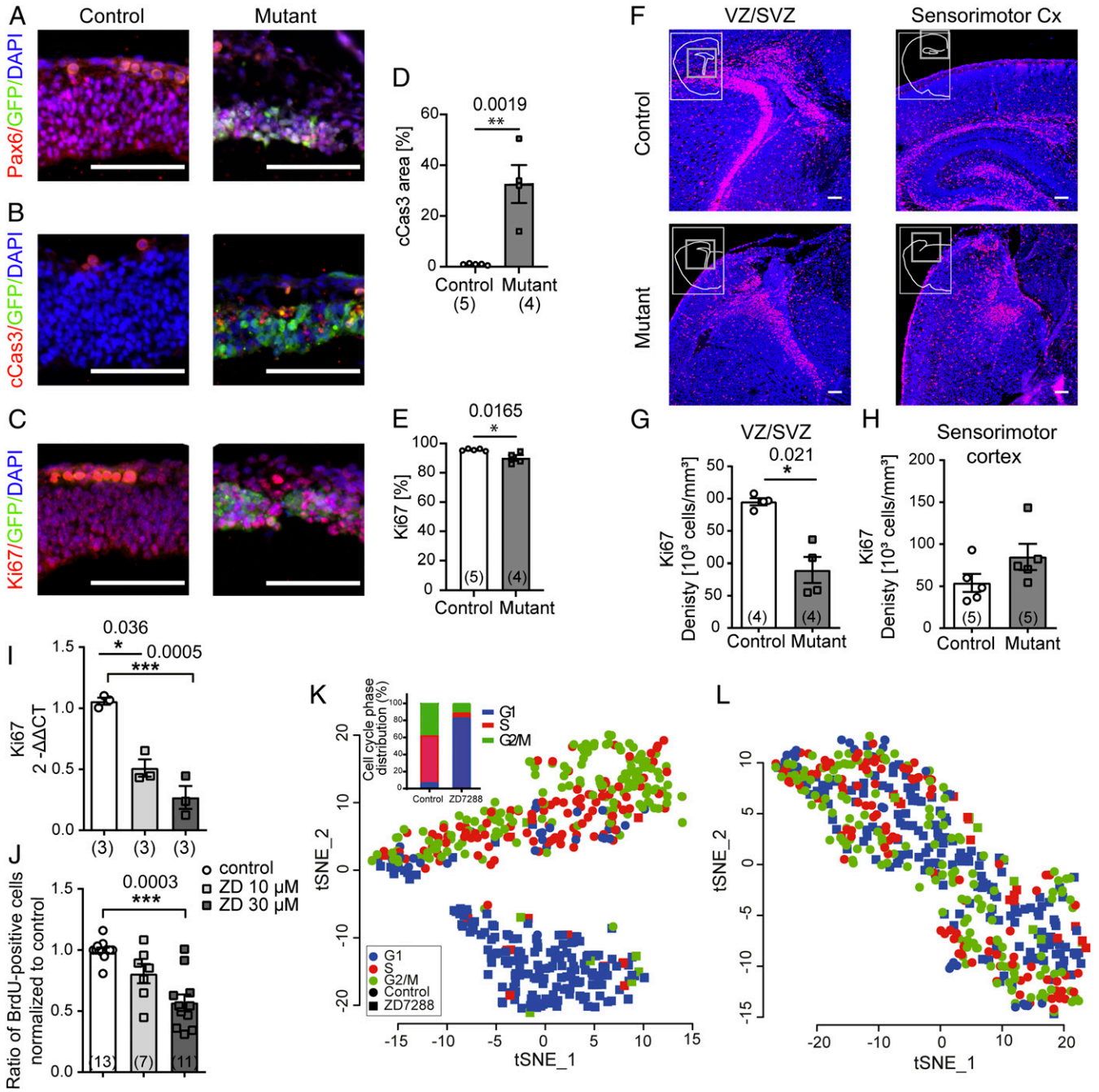

Fig. 3. Impact of I_h blockade on proliferation and cell cycle state. (*A–C*) Cortical sections of E12.5 control and EMX1-HCN-DN mutants stained for (*A*) radial glia cells (Pax6, red), (*B*) apoptotic (cleaved Caspase-3; cCas3, red), and (*C*) proliferating cells (Ki67, red); eGFP is depicted in green, DAPI in blue. (*D*) Quantification of cCas3-positive area in percentage of total area analyzed (unpaired Student's *t* test). (*E*) Quantification of Ki67-positive cells in percentage of DAPI-positive cells (unpaired Student's *t* test). (*F*) Images are representative of Ki67 (red) staining of the VZ/SVZ and the sensorimotor cortex in P0 control mice and EMX1-HCN-DN mutants; DAPI is shown in blue. (*G* and *H*) Quantification of Ki67 expression (unpaired Student's *t* test). (*I* and *J*) Analysis of Ki67 mRNA level (*I*) and BrdU incorporation (*J*) in rat NSCs treated with ZD7288 (10 and 30 µM; Ki67: one-way ANOVA with Tukey's post hoc; BrdU: Kruskal–Wallis with post hoc Dunn's test). (*K*) Two-dimensional, tSNE projection of scRNA-seq data from vehicle-treated control (circles, 281 cells), and ZD7288-treated (30 µM, square, 190 cells) rat NSCs. The cell cycle phase of each cell, which was determined from its gene expression profile, is indicated by the legend (*Lower Left*). (*Inset*) Relative distribution of cell cycle phases in the vehicle-treated (control) and ZD7288-treated NSC groups, which were significantly different from each other ($P < 0.0001$, χ^2). (*L*) tSNE projection of the same NSCs as in *K* after regressing out the variance explainable by cell cycle gene transcripts. (Scale bars, 100 µm.) Data are presented as mean ± SEM; *n* is given in parentheses; *P* values are above asterisks. Images in *A–C* are representative of 5/4 animals, and *F* are representative examples of *G* and *H*.

lower ratio of immature neurons 5 d after FGF2 withdrawal (Fig. 4 *E–H*), we observed early expression of the glial markers GFAP and CNPase in sections from P0 EMX1-HCN-DN mutants (Fig. 4 *A–D*), suggesting that in these animals, the switch between neurogenesis and gliogenesis might have prematurely occurred. In contrast, GFAP and CNPase expression levels in adult EMX1-HCN4-573X and NEX-HCN-DN mutants were indistinguishable from those in controls (*SI Appendix*, Figs. S7 and S8). These results

Table 1. Gene set enrichment analysis of KEGG pathways

KEGG ID	Pathway	DE ratio	Background ratio	Enrichment	*P* adj.
rno03030	DNA replication	19/212	36/8,351	20.79	2.63×10^{-19}
rno04110	Cell cycle	25/212	127/8,351	7.75	6.89×10^{-14}
rno03430	Mismatch repair	10/212	23/8,351	17.13	5.30×10^{-9}
rno04115	p53 signaling pathway	12/212	70/8,351	6.75	7.87×10^{-6}
rno03420	Nucleotide excision repair	10/212	47/8,351	8.38	8.45×10^{-6}
rno03040	Spliceosome	16/212	138/8,351	4.57	1.26×10^{-5}
rno04114	Oocyte meiosis	13/212	115/8,351	4.45	0.0002
rno00970	Aminoacyl-tRNA biosynthesis	9/212	69/8,351	5.14	0.0014
rno03013	RNA transport	14/212	168/8,351	3.28	0.0021
rno04218	Cellular senescence	14/212	189/8,351	2.92	0.0064
rno00260	Glycine, serine, and threonine metabolism	6/212	40/8,351	5.91	0.0087

indicate that, in addition to—and perhaps as a consequence of—a direct effect on NSC proliferation, a dysfunction in HCN subunits might also result in a dysregulated balance between neurogenesis and gliogenesis. A recent study found that both the application of ZD7288, or of the less specific I_h blocker Cs^+, onto NSC cultures reduced the fraction of cells showing spontaneous Ca^{2+} oscillations (23). Using slightly different experimental conditions such as a shorter observation time, we did not find systematic changes in Ca^{2+} oscillations in our experiments with cultured rat NSCs upon ZD7288 application (*SI Appendix*, Fig. S6 *H* and *I*). ZD7288 is the most commonly used pharmacological I_h inhibitor that can show concentration-dependent off-target effects on T-type calcium channels or voltage-gated sodium channels (43–45). While voltage-gated calcium currents can be detected in neural stem and progenitor

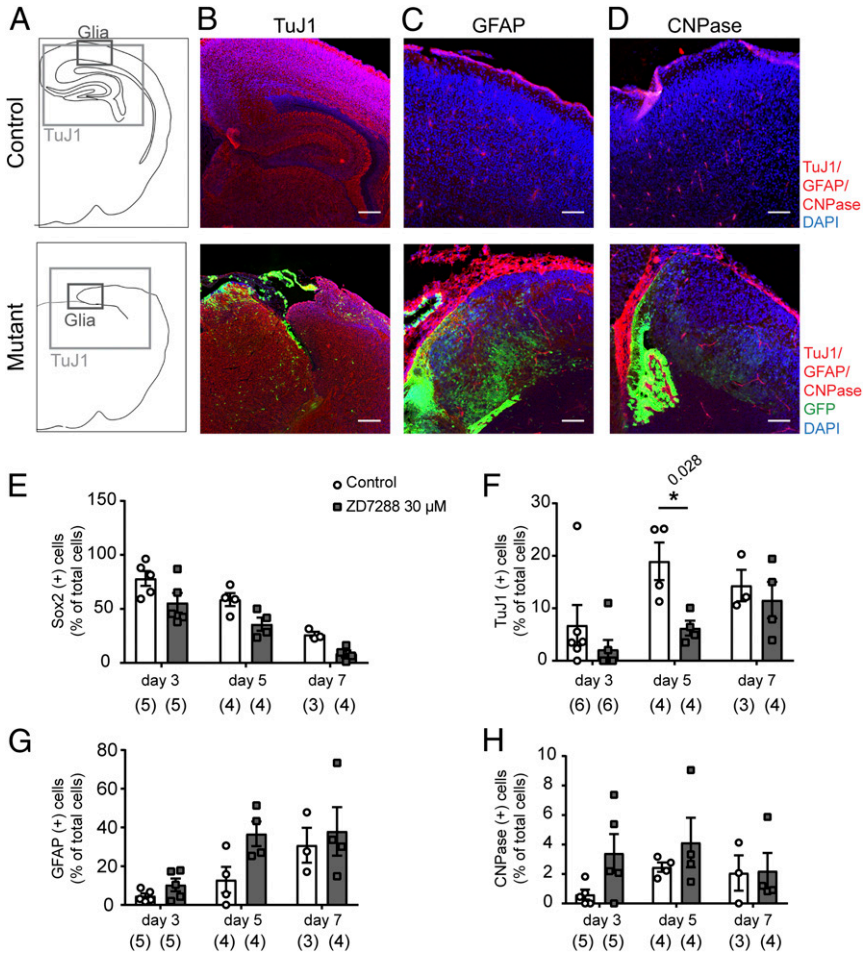

Fig. 4. Influence of I_h ablation on differentiation in cultured NSCs and P0 mouse brains. (*A*) Schematic drawing of coronal sections with the region highlighted that is shown in the following sections. Immunofluorescence detection of (*B*) neurons (TuJ1), (*C*) astrocytes (GFAP), and (*D*) oligodendrocytes (CNPase) in the EMX1-HCND-DN (mutant) neonatal brain compared to those in controls. (*E–H*) Cortical stem cells differentiated in the absence of FGF2 were analyzed at days 3, 5, and 7 after FGF2 withdrawal (Mann–Whitney *U* test). (*E*) The percentage of cells expressing the neural stem cell marker Sox2, (*F*) the neuronal marker Tuj1, (*G*) the astrocyte marker GFAP, and (*H*) the oligodendrocyte marker CNPase. For images representative of the differentiated cell cultures, see *SI Appendix*, Fig. S11. (Scale bars for *B*, 200 μm, and for *C* and *D*, 100 μm.) Data are presented as mean ± SEM; *n* is given in parentheses; *P* values are above asterisks. Images in *B* are representative of one experiment and in *C* and *D* of three similar experiments.

cells, only L-type calcium channels have hitherto been identified, which are not known to be blocked by ZD7288 (46–48). Furthermore, voltage-gated sodium channels are primarily associated with the differentiation, but not proliferation, of neural progenitor cells (47–54). Therefore, both the dominant-negative transgenic strategy and the pharmacological block of I_h are likely to have affected the same HCN current-dependent mechanism.

HCN channels are part of an evolutionarily old and conserved family of ion channels (55) that are expressed in different cell types with proliferative potential (56, 57). A comparison of our HCN subunit expression analyses with those of other studies and databases of embryonic mouse brain, stem cells, and induced human pluripotent stem cells has consistently revealed HCN3 to be the most abundant subunit (21, 23, 27, 56, 57). In addition to HCN3, the data also implicate HCN1 and HCN4 as potential HCN subtypes in the developing mouse and human fetal cerebral cortices (*SI Appendix*, Figs. S1 and S2). The endogenous expression of all four HCN subunits and their potentially heteromeric channel assembly can be targeted by our dominant-negative approach in which I_h is inhibited in a subunit-independent manner. The low abundance of all HCN subunits and the marked phenotypes resulting from the loss of HCN channel activity suggest a transient but essential function during the cell cycle. This transient, low abundance of HCN transcripts, together with the different experimental methods, fluorescence-activated cell sorting–sorted cells with bulk RNA-seq (*SI Appendix*, Fig. S1), well-based scRNA-seq platform with low cell number but increased sequencing depth (dataset I), and droplet-based scRNA-seq with higher cell number but lower sequencing depth (dataset II), led to varying numbers of cells expressing any HCN subunits. Furthermore, one major limitation to the scRNA-seq experiments is the probabilistic approach resulting in a potential underrepresentation of transcripts with generally low abundance, like those of ion channels, as their protein turnover is very slow.

Prenatal expression of the HCN1 subunit, which is affected by mutations in microcephalic EIEE patients (10, 11), started to increase at mid-gestation and was almost adult-like as early as at birth and during the first year of life (ref. 25 and *SI Appendix*, Fig. S2). The expression pattern of *HCN1* in the developing human neocortex is, thus, in line with a role in late embryonic/fetal and neonatal/early infantile brain development.

Brain malformation such as polymicrogyria is among the defects associated with ion channels, including NMDAR (here GRIN1, GRIN2B) (58, 59) or with voltage-gated sodium channels (SCN3A) (60). Previous publications show that the NMDA receptor is mainly expressed in migrating neurons, while the SCN3A gene is prominently expressed in the human-specific cell population of the outer radial glia cells and intermediate progenitor cells (60–62). This observation suggests an effect on mainly the migration of early neurons, or on specific proliferative populations, designed to expand the cell numbers for the advanced gyrified human neocortex. In addition to causing polymicrogyria, different mutations in the NMDAR subunits can result in secondary microcephaly, which is potentially due to either apoptosis by nonmigrated neurons or glutamate excitotoxicity caused by gain-of-function mutations (58, 59).

The differential gene expression analyses from our scRNA-seq datasets comparing untreated and ZD7288-treated NSCs revealed a substantial overlap with genes identified in Elp3cKO mice, in which increased UPR in apical precursors affected indirect neurogenesis (via intermediate progenitors) (6). It is tempting to speculate that the marked apoptosis at E12.5 in our EMX1-HCN-DN mouse model is a downstream consequence of a slowed cell cycle progression and subsequently increased UPR. The more pronounced microcephaly in our model as compared to the Elp3cKO model may indicate that the loss of HCN channel function affected both direct and indirect neurogenesis by inducing, for example, also earlier progenitor depletion by apoptosis. Furthermore, the reduced proliferation of neural progenitors (Fig. 3) is attributable to a severe reduction in cell cycle speed, which, as our scRNA-seq data indicate, is primarily due to G1 phase lengthening, ultimately causing depletion of the neural progenitor pool and, as a consequence, microcephaly. Loss of functional HCN channels in NSCs affected the membrane potential (23), which is more depolarized in cycling cells than in cell cycle–exiting cells (3). Together, the data indicate that I_h, which contributes to rhythmic activity in many cell types likely including NSCs (23), also helps control the entry into or exit from the cell cycle in neural progenitors. This hypothesis is in line with recent findings showing that experimental hyperpolarization of the progenitor cell pool causes their premature shift to later developmental stages (6), thus highlighting the importance of bioelectrical membrane properties as determinants of cell proliferation and differentiation. While target genes of the Wnt signaling pathway were enriched among (mostly up-) regulated genes in the respective progenitors in that study (6), we did not find Wnt signaling target gene enrichment among differentially regulated genes in our NSC cultures after pharmacological I_h blockade, which argues for Wnt-independent mechanisms. As I_h inhibition with ZD7288 led to a reduction in proliferation, not only in NSCs (our study and ref. 23) but also in embryonic stem cells (21, 22), HCN subunit–mediated currents may be part of a conserved mechanism that is not restricted to brain development. In this context, it is noteworthy that HCN1 channel expression is also controlled by REST/NRSF, the critical epigenetic regulator of neurogenesis. REST/NRSF is expressed in embryonic and neural stem cells and is essential for maintaining NPC fate by inhibiting neuronal-specific genes (63, 64). Dysregulation of REST/NRSF through the deficiency of its upstream regulator ZNF335 resulted in microcephaly in both humans and mice (65). The forebrain-specific, EMX1-cre–mediated knockdown of ZNF335 in mice disrupted progenitor cell proliferation, cell fate, and neuronal differentiation and—similar to the phenotype of EMX1-HCN-DN mice—caused a severe reduction in forebrain structure (65). Although REST/NRSF controls many genes (66), its dysregulation may result in the suppression of HCN1 channel expression at a critical cell cycle checkpoint and, thus, contribute to the observed phenotypes in mice and humans.

Although causality is difficult to prove in patients carrying *HCN1* mutations that are associated with EE and microcephaly (10, 11), the combined clinical and experimental data indicate that HCN channel dysfunction–mediated impairment of neural progenitor proliferation is a mechanism that warrants further investigation into idiopathic brain malformations.

Materials and Methods

Animals and Husbandry. All experimental procedures were approved by the Behörde für Gesundheit und Verbraucherschutz of the city-state of Hamburg and by the Landesamt für Natur, Umwelt und Verbraucherschutz Nordrhein-Westfalen, Germany. Animals were kept in Type II long (Tecniplast) plastic cages under standard housing conditions (21 ± 2 °C, 50 to 70% relative humidity, food, and water ad libitum and nesting material provided). Mice were kept on an inverted 12:12 light:dark cycle.

In the EMX1-HCN-DN mouse lines, mainly EMX1-Cre– or HCN-DN–negative animals were used as controls.

Generation of Rosa26(loxP-stop-loxP-tTA2)^{lsb} Mice. A floxed stop cassette (67) was inserted 5′ of the tTA2 coding sequence (Clontech) into the plasmid pcDNA3 (Invitrogen), and the resulting loxP-Stop-loxP-tTA2-BGH-poly(A) fragment was excised and inserted into the pBigT vector (68). Subsequently, the AscI–PacI insert of pBigT was isolated and inserted into the pROSA26-PA vector (68), resulting in the target vector pROSA26-stop-tTA2. The linearized targeting vector was electroporated into R1 embryonic stem (ES) cells, which were subjected to selection by geneticin (G418, Invitrogen). Homologous recombination was verified by Southern blot analysis of digested genomic ES cell DNA.

Generation of Mice Expressing HCN-DN and HCN4-573X. Transgenic mice carrying the pBI-HCN-DN/eGFP construct (Tg(BitetO-HCN4$^{p.G480S}$, eGFP)$^{C\ lsb}$) or mice carrying the pBI-HCN4-573X/eGFP construct (Tg(BitetO-HCN4$^{p.573X}$,eGFP)$^{C\ lsb}$)

were generated by pronuclear injection using standard techniques. Founder mice and the resulting offspring were genotyped by PCR using ear or tail biopsies, backcrossed to the C57BL/6J (B6) background for more than 10 generations, and crossed with promoter mice B6-Tg(Emx1$^{tm1(cre)Ito}$) (35), B6- Tg(Nex-cre (NeuroD6$^{tm1(cre)Kan}$)) (37), or B6-Tg(CaMKIIα-tTA)$^{1Mmay/J}$ (69). Control animals lacked at least one (40% were negative for the EMX1-Cre allele, and 49% were negative for HCN-DN) or two alleles (3% were negative for the tTA2 and HCN-DN alleles, and 6% were negative for EMX1-Cre and HCN-DN). To suppress HCN-DN expression, mice received 200 mg doxycycline per kg chow or drinking water. For/In the EMX-HCN-DN +dox cohort, doxycycline was administered until the day of birth.

For cloning of the HCN constructs and genotyping protocols please refer to *SI Appendix, Supplementary Materials and Methods*.

Tissue Preparation for Histology Mice were deeply anesthetized with a combination of ketamine and xylazine (100 mg/kg ketamine, Ketanest; Pfizer and 20 mg/kg xylazine, Rompun; Bayer) and transcardially perfused with phosphate-buffered saline (PBS), followed by phosphate-buffered 4% formaldehyde (PFA) solution (Histofix, Carl Roth). Brains were dissected and postfixed in 4% formaldehyde (FA) for 24 h and cryoprotected in 15 and 30% sucrose in PBS overnight, respectively. Tissue was rapidly frozen using optimal cutting temperature compound (OCT) and cut into 14-μm-thick slices on a cryostat (CM 3050S, Leica). Tissue and slices were stored at −80 °C.

Embryos were dissected and staged according to Theiler's staging criteria at approximately embryonic day E12.5 (TS19-20). The embryonic heads were immersion fixed in 4% PFA solution and cryoprotected in 30% sucrose. The tissue was frozen in OCT and cut into 12-μm-thick slices.

Fluorescent Nissl Stain. The NeuroTrace 530/615 Red Fluorescent Nissl Stain (Molecular Probes) was diluted 1:25 in PBS and applied according to the manufacturer's protocol.

Immunohistochemistry. Slides were washed three times in PBS for 5 min. Antigen retrieval was performed in 10 mM sodium citrate buffer (pH 9) at 70 °C for 30 min for CNPase and cleaved Caspase 3 staining. After cooling to room temperature in the buffer, slides were washed four times each in PBS for 5 min. The blocking of nonspecific binding was performed at room temperature for one hour. For GFAP staining, the blocking solution contained 10% normal horse serum, 0.2% bovine serum albumin, and 1% Triton X-100 solution in PBS. For CNPase, cleaved caspase-3, Ki67, TuJ1, and GFP stains, the blocking solution contained 5% normal goat serum and 0.2% Triton X-100 in PBS. The primary antibody (Ki67: rabbit, AB15580, Abcam, 1:250; TuJ1: mouse, MAB1195, R&D Systems, 1:100; GFAP: mouse, clone GA5, MAB3402, Millipore, 1:500; CNPase: mouse, Clone 11–5B, C5922' Sigma-Aldrich, 1:1,000; cleaved Caspase 3: rabbit, AF835, R&D Systems, 1:2,000; GFP: conjugated with A488, rabbit, A-21311, Life Technologies, 1:200) was diluted in PBS and applied overnight at 4 °C. Brain slices were washed four times in PBS for 5 min and incubated for 2 h in the secondary antibody (1:200 Alexa Fluor 546/488 goat anti-mouse (A-11030) or in goat anti-rabbit (A-11035) IgG, Molecular Probes) in PBS at room temperature. HCN4 detection was performed using a phosphate buffer (PB) (12 M Na_2HPO_4, 5 M NaH_2PO_4, pH 7,4) for washing steps and the 2-h-long block in 5% Chemiblocker (Millipore), 0.5% Triton X-100 in PB. The primary antibody was diluted 1:100 in PBS (HCN4: mouse, 75–150, NeuroMab). Further processing was performed as described above. Slides were washed four times in PBS for 5 min and embedded in DAPI Fluoromount-G (Southern Biotech).

Sections from E12.5 embryonic brains were heated in Tris-EDTA (5mM Tris HCl, 1mM ethylenediaminetetraacetic acid [EDTA], pH 8) antigen retrieval buffer at 99 °C for 20 min followed by a 20-min cool down at room temperature (RT). After a 5-min PBS rinse, the sections were blocked in 10% normal donkey serum and 0.3% Tween 20 solution in PBS for 1 h. Primary antibodies (Pax6: rabbit, 901201, Biolegend, 1:1,000; cleaved Caspase 3: rabbit, D175 [A51E], Cell Signaling, 1:2,000; Ki67: mouse, 556003, BD Bioscience, 1:1,000; and GFP: goat, 600–101-215, Rockland, 1:2,500) were accordingly diluted in 0.3% Tween 20 in PBS and incubated overnight at 4 °C. Secondary antibodies (Donkey anti-rabbit IgG [H+L] Alexa Fluor Plus 555 [A32794], Donkey anti-mouse IgG [H+L] Alexa Fluor Plus 555 (A32773), Donkey anti-goat IgG [H+L] Alexa Fluor Plus 488 [A32814], Invitrogen) were diluted 1:1,000 in 10% normal donkey serum and 0.3% Tween 20 in PBS and incubated for 2h at RT. For DAPI staining (D1306, Invitrogen), the slides were washed for 10 min in a 1:50,000 dilution in PBS and mounted with Prolong Glass Antifade Mountant (P36980, Invitrogen).

Stereology. Stereological analyses were performed with a Nikon, or a Zeiss AX10, microscope equipped with StereoInvestigator software (Microbrightfield). For proliferation and apoptosis studies, four sections spaced 84 μm, approximately between +2.31 and +3.75 mm from the olfactory bulbs, were analyzed and, according to the developmental mouse brain atlas, represent the sensorimotor cortex and the underlying VZ/SVZ (70). The optical dissector principle was used to estimate cell densities as described (71). The parameters of analysis were as follows: guard space depth was 2 μm, base and height of the dissector was 3,600 μm^2 and 10 μm, respectively, and the distance between the optical dissectors was 60 μm, objective 40× PlanNeofluar 40×/0.75 (Zeiss). For the analysis of migration, five sections, 56 μm apart from each other, were studied. The electroporated area was subdivided into layers two/three (target region), layers four to six, subplate and intermediate zone (migration region), and VZ/SVZ as a proliferative (starting) region. All electroporated cells in the regions of interest were counted.

Image Analysis E12.5 Embryos. All images were taken using a Leica DM5500 B with a Leica DFC 360 FX camera. For analysis, FIJI Is Just ImageJ software (v1.53g) was used. All sections were matched on an anterior–posterior and on a medial–lateral axis. For Ki67 cell numbers, DAPI- and Ki67-positive cells were manually counted in a 140-μm-long fragment of the cortex. To establish the cleaved Caspase 3–positive area, a 140-μm-long area was drawn along the cortex and processed by using the "Triangle" threshold settings and "Analyze Particle" function (size: 0 to infinity, circularity: 0 to 1). The percentage of thresholded area to total region of interest was calculated. Four sections per embryo were analyzed.

Magnetic Resonance Volumetry. For MRI, neonatal animals were deeply anesthetized using a combination of ketamine (100 mg/mL) and xylazine (20 mg/mL). Subsequently, they were perfused with 7 mL PBS followed by 4% FA. Both solutions contained 3% gadolinium as an MRI contrast agent. The head was fixed overnight in FA gadolinium solution and stored in 3% gadolinium in PBS until measurement. The MRI was performed on a 7.0 T small animal scanner with a three-dimensional protocol (ClinScan, Bruker). Neonatal animals were analyzed with turbo spin-echo [repetition time (TR) 200 ms, echo time (TE) 8.5 s, turbo factor 8, matrix 144 × 192 pixels, field of view (FOV) 11 × 14 mm, slice thickness 80 μm]. Animals that were 3 wk old were measured alive under 1 to 2% isoflurane anesthesia (500 mL/min). Both the breathing rate and body temperature of the head-fixed animals were continuously monitored. The juvenile animals were imaged using a constructive interference in steady state sequence (TR 8.14 ms, TE 4.07 s, matrix 192 × 192 pixels, FOV 16 × 16 mm, slice thickness 90 μm). All further analyses were performed with Osirix (Pixmeo SARL). For quantitative analysis, the brain volumes included the midbrain but not the cerebellum because the respective boundaries were reproducibly identified both in the control and EMX1-HCN-DN mice.

Immunoblots. Tissue samples were homogenized in a solution containing 330 mM sucrose, 20 mM 3-(*N*-morpholino) propane sulfonic acid (MOPS), 1 mM (EDTA), and a proteinase inhibitor mixture (Sigma-Aldrich). Membrane proteins were separated from cytosolic proteins by ultracentrifugation or a ProteoExtractR Transmembrane Protein Extraction Kit (Novagen). Protein concentration was measured with a bicinchoninic acid protein assay (Thermo Scientific) according to the user manual. Proteins were separated using 12% Bis-Tris sodium dodecyl sulfate–polyacrylamide gel electrophoresis in MOPS buffer. The blotting of proteins on the nitrocellulose membrane was performed in NuPAGE (Life Technologies) transfer buffer containing methanol. The total protein content on the membrane was determined using SERVAPurple staining (Serva) according to the manufacturer's protocol. For immunostaining, all solutions were prepared with Tris-buffered saline (TBS) containing 0.01% Tween 20. The membrane was washed in TBS solution and blocked in 5% milk powder. The primary antibody was diluted 1:2,000 for HCN subunit detection and 1:500 for HA staining (HCN1: mouse, N70/28, NeuroMab; HCN2: mouse, 75–111, NeuroMab; HCN3: mouse, 75–175, NeuroMab; HCN4: mouse, 75–150, NeuroMab; and HA: mouse, 12CA5, Roche) in 1% milk powder and incubated overnight at 4 °C. The membranes were washed for 4 × 5 min and incubated with horseradish peroxidase (HRP)–coupled secondary antibody (1:500) for 1 h at RT. For detection, Luminata Crescendo Western HRP Substrate (Millipore) was used.

In Situ Hybridization. To detect transgenic hHCN4-DN, a construct (polyA)-specific, α-32S-UTP (~800 Ci/mmol)-labeled probe of 445–base pair (bp) length within exon 8 of the hHCN4 (3,148 to 3,592 bp) was used. The in situ hybridization experiments were performed using standard techniques.

qPCR. To analyze the HCN subunit expression during different developmental changes, the TissueScan Mouse Developmental Tissue qPCR Array (Origen) was used. A TaqMan-PCR was performed with a commercially available primer and probe mix containing VIC™ (2′-chloro-7′-phenyl-1,4-dichloro-6-carboxy-fluorescein)

glyceraldehyde-3-phosphate dehydrogenase (GAPDH) probe (GAPDH: Mm99999915_g1), and FAM™ (6-carboxyfluorescein) HCN subunit probe (HCN1: Mm00468832_m1; HCN2: Mm00468538_m; HCN3: Mm01212852_m; HCN4: Mm01176086_m1; Applied Biosystems). A 7900HT Fast Real-Time PCR System (Applied Biosystems) instrument was used to perform the PCR. Data were analyzed with SDS 2.3, RQ Manager 1.2, and DATA Assist version 2.0 (Applied Biosystems). Individual reactions were normalized to coamplified GAPDH. For illustration, all time points were normalized to E13 of the respective HCN subtype.

RNA-Seq. The detailed methods of the cell type–specific transcriptome analysis were published elsewhere (26), and the dataset was reanalyzed for HCN subtype expression levels. To identify the HCN subtypes, the sequences were aligned with the mouse reference genome (mm10) and the human genome (hg19). The data are shown in fragments per kilobase per million reads with a threshold of 1.

Single-cell RNA-seq analysis of cultured NSCs isolated from the cortex of E14.5 Sprague Dawley rats (NSC001, R&D systems; cultured according to the manufacturer's protocol) was performed according to the manufacturer's protocols with two independent methods using either a well-based approach with four biological and one technical replicate using the WaferGen ICELL8 single-cell system (dataset I) or a drop-seq approach with the 10x chromium system (dataset II, 10X Genomics).

For the ICell8 approach, the indexed amplified cDNA was collected using a collection kit (WaferGen) and centrifuged at 3,220 *g* for 10 min at 4 °C. After concentrating the product with a DNA Clean & Concentrator Kit (Zymo Research), the cDNA was purified with 0.6× AMpure XP beads (Beckman). The quality of the cDNA was assessed on a Tape 12 Station (Agilent). A total of 1 ng purified cDNA was used as starting material for the library preparation. The cDNA was tagmented by Nextera XT transposome, and adapter sequences were successively added to the end of the fragments. In a subsequent step, amplification was carried out by PCR. The library was purified using a 1:1 ratio of AMpure XP beads followed by dual Solid Phase Reversible Immobilization treatment.

The libraries from the 10X experiment were prepared with the Chromium Single Cell 3′ Library & Gel Bead Kit version 2 and i7 Multiplex Kit (10X Genomics).

Finally, the quality and molar concentration of the library were assessed on a Tape Station. Sequencing was performed on an Illumina HiSeq 4000.

For dataset II, Cell Ranger Suite (version 3.0.2, 10X Genomics) was used to perform sample multiplexing, barcode processing, and the generation of a single-cell gene UMI (unique molecular index) count matrix.

Single-Cell Transcriptome Analysis. In total, the read count matrix of dataset I contains 129,136,294 reads, each read with one out of 510 molecular barcodes. After a quality control of the reads using FastQ Screen (https://www.bioinformatics.babraham.ac.uk/projects/fastq_screen/), we obtained distinct RNA profiles for 510 barcodes, including five positive controls (total RNA from bulk samples of nontreated cells) and five negative controls (empty well samples). After removing the controls, we obtained a matrix of 500 barcodes (corresponding to cells) × 23,425 ENSEMBL IDs (corresponding to genes).

All barcodes were required to comprise at least 200 different detectable genes (at least one count). This requirement was met for all barcodes. Subsequently, we removed the genes that were detected (at least one count) in fewer than seven cells. This left us with 14,588 genes. Based on the distribution of total counts per barcode, we removed all cells with more than 2^{20} counts because they potentially originated from wells containing multiple cells (*SI Appendix*, Fig. S12).

Dataset II contained 849,391,962 total reads from 4,691 cells, with a total of 25,399 detected genes. For further analysis, we considered only cells expressing 2,000 to 6,000 genes (with at least one UMI count) and genes expressed in at least three cells. We additionally removed cells containing more than 11% mitochondrial gene counts. The final UMI count matrix consisted of 3,492 cells and 13,802 genes.

All downstream analyses were performed using in-built functions from the Seurat Bioconductor package (72). Seurat assigns a cell cycle phase (G1, S, or G2/M) to each cell. To this end, we had to provide a list of cell cycle marker genes for S and G2/M (Dataset S2) and performed t-distributed stochastic neighbor embedding mapping (t-SNE) to a two-dimensional space before and after cell cycle gene removal using the RegressOut function in Seurat. Differential gene expression analysis between groups was done using the Wilcoxon rank-sum test. Enrichment analysis of differentially regulated KEGG pathways was done using ClusterProfiler (73), and we employed TopGO (74) for Gene Ontology enrichment analysis.

Dataset III was downloaded from http://mousebrain.org/downloads.html (27) and contains all scRNA-seq data from forebrain cells prepared from E9.0 to E14.0 embryos (forebrain: E9.0, E10.0, E11.0; forebrain dorsal: E12.0, E12.5; forebrain ventral: E12.0, E13.0). The original dataset contained scRNA-seq data from 292,495 total cells with a total of 31,053 genes detected. After selection with respect to brain region and age, our subsequent quality control removed cells with less than 200 or more than 6,000 genes detected per cell. Cells with a mitochondrial transcript content of >15% were also removed. The final library contained 47,263 cells with a total of 31,053 genes detected with a 6,153 median UMI counts per cell. The cell-type assignment was based on molecular marker expression (*SI Appendix*, Table S1) to detect the major cell types present in late embryonic mouse brain. For the counting of *Hcn1-4* isoform-expressing cells, at least one UMI count per cell had to be detected.

Cell Culture. For primary NSC monolayer culture, rat cortices were derived from embryonic day 13.5 as described previously (75). Details are given in *SI Appendix, Supplementary Materials and Methods*.

In Vitro Proliferation Assays. For proliferation analysis, qPCR for Ki67 was performed. The GeneUp Total RNA Mini Kit (Biotechrabbit) was used for extracting the RNA from cortical stem cells. RNA amount was measured with the GeneQuant 1300 and transcribed into cDNA using the QuantiTect Reverse Transcription Kit (Qiagen). qPCR was performed with the KAPA SYBR FAST Universal Kit (Peqlab) and analyzed with the RotorGene RG-3000 (Corbett Research) using Ki67 primer (forward: TCT TGG CAC TCA CAG TCC AG; reverse: GCT GGA AGC AAG TGA AGT CC; Biolegio) and RPL13 as housekeeping gene (forward: TCT CCG AAA GCG GAT GAA CAC, reverse: CAA CAC CTT GAG GCG TTC CA; Biolegio). For BrdU experiments, 10 μM BrdU (Fluka) was added to the cell culture medium for 6 h before fixation with 4% PFA for 10 min. For DNA denaturation, 2 M HCl was used for 30 min. Anti-BrdU antibody (mouse, clone BU-33, B8434, Sigma-Aldrich) was diluted 1:100.

Immunocytochemistry. To analyze the differentiation in cell culture, Sox2 was used as a neuronal stem cell marker (mouse, MAB2018, R&D Systems, 1:100), Tuj1 (mouse, MAB1195, R&D Systems, 1:100) as a marker for early neurons, GFAP (rabbit, 180063, Invitrogen, 1:1,000) for astrocytes, and CNPase (mouse, clone 11–5B, MAB326, Millipore, 1:5,000) for labeling oligodendrocyte precursor cells. Fluorescein-labeled anti-mouse or anti-rabbit IgG (1:200, Invitrogen) was used as a secondary antibody. The HCN subtypes were detected using the following antibodies (1:100): HCN1: mouse, N70/28 (NeuroMab); HCN2: mouse, 75–111 (NeuroMab); HCN3: mouse, 75–175 (NeuroMab); and HCN4: mouse, 75–150 (NeuroMab) followed by Alexa Fluor 546 goat anti-mouse IgG (A-11030, 1:200, Molecular Probes).

For immunocytochemical stainings, cells were washed with PBS and fixed with 4% PFA for 10 min. After washing with PBS, cells were permeabilized and blocked in 0.1% Triton X-100 and 10% normal goat serum in PBS. The primary antibody, diluted to optimal working concentration, was applied overnight in 3% goat serum at 4 °C. Cells were washed with PBS followed by secondary antibody incubation (1 h at RT) with fluorescein-labeled anti-mouse IgG (1:200, Invitrogen) in 3% normal goat serum in PBS. Cells were counterstained by a 5-min incubation in Hoechst 33342 (Invitrogen) diluted 1:500. Slides were mounted using Fluoromount (Southern Biotech). All microscopic investigations were performed with an inverted fluorescent phase-contrast microscope (Keyence BZ-9000E). From each well, 10 images were randomly chosen and taken for analysis.

Antibody Validation. All antibodies used are commercially available and were selected for their specificity according to the manufacturer's validation. For staining with each antibody, we additionally performed appropriate negative controls (omission of the primary antibody or substitution by the normal serum from the animal in which the antibody was raised).

Electrophysiological Recordings. For validation of the dominant-negative effect of the HCN-DN transgene on I_h in CA1 pyramidal neurons, 9- to 12-wk-old B6-Tg (CaMKIIα-tTA$^{1Mmay/J}$, (BitetO-HCN$^{p.G480S}$, eGFP)$^{C\ Isb}$)) mice were used. Coronal hippocampal slices (300 μm) of adult mice were sectioned after intracardial perfusion with ice-cold sucrose-artificial cerebrospinal fluid (ACSF) (50 mM sucrose, 75 mM NaCl, 25 mM $NaHCO_3$, 2.5 mM KCl, 1.25 mM NaH_2PO_4, 0.1 mM $CaCl_2$, 6 mM $MgCl_2$, and 2.5 mM glucose, oxygenated with 95% O2/5% CO_2). After 60 min of recovery, slices were transferred to a recording chamber and continuously perfused at 2 to 4 mL · min^{-1} with oxygenated ACSF (2.5 mM glucose and 22.5 mM sucrose) at 36 °C. Fast excitatory and inhibitory synaptic transmission was inhibited by 20 μM 6-cyano-7-nitroquinoxaline-2,3-dione and 10 μM gabazine. CA1 pyramidal neurons were visualized by infrared differential interference contrast video microscopy and epifluorescence for the detection of

eGFP. Whole-cell patch recordings, data acquisition, and analysis were essentially performed as described (76).

Details for the electrophysiological recordings from primary cortical stem cells are given in *SI Appendix, Supplementary Materials and Methods*.

Statistical Analyses. Statistical analyses were performed using GraphPad Prism software version 7.02. A single experiment (n) was defined as data points from one mouse or one well (10 images/well) for cell culture experiments. All data were tested for their normal distribution (D'Agostino and Pearson or Shapiro–Wilk normality tests) and, when appropriate, for variance of distribution (F test; Brown–Forsythe). For single comparisons, an unpaired two-tailed Student's t test or a Mann–Whitney U test was performed. All tests were two tailed. For multiple comparisons, a two-way ANOVA or one-way ANOVA was employed. Post hoc analysis with the honest Tukey's significant difference test was subsequently performed when appropriate. For nonparametric testing, Kruskal–Wallis one-way ANOVA with post hoc Dunn's test was performed. For distribution analyses, χ^2 test was used. The sample size in each experiment was determined based on the previous publications using a similar experimental setting conforming to ethical guidelines for animal research. No randomization method was used. Unless specified otherwise, group measures are given as mean ± SEM with a significance annotation of $*P < 0.05$, $**P < 0.01$, $***P < 0.001$, and $****P < 0.0001$, and significance was set at $P < 0.05$.

Data Availability. scRNA-Seq data have been deposited in the Gene Expression Omnibus (accession no. GSE181980). Previously published data were used for this work (three published datasets of the following studies were reanalyzed by us with a focus on HCN channel subunits. The origin of the data and references to the original studies are given in the paper. Ref. 26: *SI Appendix*, Fig. S1 *D* and *E*; ref. 27: *SI Appendix*, Figs. S1 *F–H* and S8; and ref. 25: *SI Appendix*, Fig. S2.

ACKNOWLEDGMENTS. We thank Kathrin Sauter for technical assistance with mouse line generation and genotyping, Dr. Irm Hermans-Borgmeyer for transgenic services, Dr. Axel Neu (University Medical Center Hamburg-Eppendorf, UKE, Germany) for help with cell culture patch-clamp experiments, Dr. Jan Sedlacik (UKE) for assistance with the MRI experiments, Dr. Stefan Blaschke (University Hospital Cologne) for support with the stem cell culture experiments, Dr. Christoph Möhl (Image Data Analysis Facility, German Center for Neurodegenerative Diseases) for providing the domain-detect.ijm macro for Ca^{2+} imaging analysis, Prof. Peter Nürnberg and his team (Cologne Center of Genomics, University of Cologne) for help with the scRNA-seq experiments, and Dr. Dennis Mehrkens for help with breeding experiments. We acknowledge the support of animal facilities for excellent mouse care: Hamburg: H.Voss (Center for Molecular Neurobiology Hamburg team) and Cologne: Prof. Esther Mahabir-Brenner (Center for Molecular Medicine Cologne team) and Dr. Maria Guschlbauer (Medical Faculty team). We are grateful to the authors La Manno et al. and the Linnarsson lab (Karolinska Institute, Stockholm, Sweden) for making their dataset available to the public already at a prepublication stage. Furthermore, we thank Dr. Bina Santoro (Columbia University, New York, NY), Prof. Gaia Tavosanis, Prof. Paolo Salomoni (German Center for Neurodegenerative Diseases, Bonn, Germany), and Prof. M. Elisabeth Ross (Weill Cornell Medicine, New York, NY) for helpful discussions and comments on the manuscript. This work was supported by grants from the German Research Foundation (IS63/3-2 and IS63/10-1 [FOR 2715: *Epileptogenesis of genetic epilepsies*] to D.I.).

1. C. C. F. Homem, M. Repic, J. A. Knoblich, Proliferation control in neural stem and progenitor cells. *Nat. Rev. Neurosci.* **16**, 647–659 (2015).
2. C. D. J. Cone, "Control of cell division by the electrical voltage of the surface membrane" in *The Twelfth Annual Science Writers Seminar American Cancer Society*, Intergovernmental Panel on Climate Change, Ed. (Cambridge University Press, Cambridge, 1970), pp. 1–30.
3. D. J. Blackiston, K. A. McLaughlin, M. Levin, Bioelectric controls of cell proliferation: ion channels, membrane voltage and the cell cycle. *Cell Cycle* **8**, 3527–3536 (2009).
4. C. D. Cone Jr, C. M. Cone, Induction of mitosis in mature neurons in central nervous system by sustained depolarization. *Science* **192**, 155–158 (1976).
5. F. C. Anda *et al.*, Cortical neurons gradually attain a post-mitotic state. *Cell Res.* **26**, 1033–1047 (2016).
6. I. Vitali *et al.*, Progenitor hyperpolarization regulates the sequential generation of neuronal subtypes in the developing neocortex. *Cell* **174**, 1264–1276.e15 (2018).
7. R. Surges *et al.*, Regulated expression of HCN channels and cAMP levels shape the properties of the h current in developing rat hippocampus. *Eur. J. Neurosci.* **24**, 94–104 (2006).
8. H. C. Lai, L. Y. Jan, The distribution and targeting of neuronal voltage-gated ion channels. *Nat. Rev. Neurosci.* **7**, 548–562 (2006).
9. H. L. Picken Bahrey, W. J. Moody, Early development of voltage-gated ion currents and firing properties in neurons of the mouse cerebral cortex. *J. Neurophysiol.* **89**, 1761–1773 (2003).
10. C. Marini *et al.*, HCN1 mutation spectrum: From neonatal epileptic encephalopathy to benign generalized epilepsy and beyond. *Brain* **141**, 3160–3178 (2018).
11. M. Lucariello *et al.*, Whole exome sequencing of Rett syndrome-like patients reveals the mutational diversity of the clinical phenotype. *Hum. Genet.* **135**, 1343–1354 (2016).
12. C. Nava *et al.*; EuroEPINOMICS RES Consortium, De novo mutations in HCN1 cause early infantile epileptic encephalopathy. *Nat. Genet.* **46**, 640–645 (2014).
13. A. Brewster *et al.*, Developmental febrile seizures modulate hippocampal gene expression of hyperpolarization-activated channels in an isoform- and cell-specific manner. *J. Neurosci.* **22**, 4591–4599 (2002).
14. K. Chen *et al.*, Persistently modified h-channels after complex febrile seizures convert the seizure-induced enhancement of inhibition to hyperexcitability. *Nat. Med.* **7**, 331–337 (2001).
15. R. A. Bender *et al.*, Enhanced expression of a specific hyperpolarization-activated cyclic nucleotide-gated cation channel (HCN) in surviving dentate gyrus granule cells of human and experimental epileptic hippocampus. *J. Neurosci.* **23**, 6826–6836 (2003).
16. S. McClelland *et al.*, Neuron-restrictive silencer factor-mediated hyperpolarization-activated cyclic nucleotide gated channelopathy in experimental temporal lobe epilepsy. *Ann. Neurol.* **70**, 454–464 (2011).
17. R. B. Robinson, S. A. Siegelbaum, Hyperpolarization-activated cation currents: from molecules to physiological function. *Annu. Rev. Physiol.* **65**, 453–480 (2003).
18. R. A. Bender *et al.*, Differential and age-dependent expression of hyperpolarization-activated, cyclic nucleotide-gated cation channel isoforms 1-4 suggests evolving roles in the developing rat hippocampus. *Neuroscience* **106**, 689–698 (2001).
19. A. L. Brewster *et al.*, Quantitative analysis and subcellular distribution of mRNA and protein expression of the hyperpolarization-activated cyclic nucleotide-gated channels throughout development in rat hippocampus. *Cereb. Cortex* **17**, 702–712 (2007).
20. R. A. Bender, T. Z. Baram, Hyperpolarization activated cyclic-nucleotide gated (HCN) channels in developing neuronal networks. *Prog. Neurobiol.* **86**, 129–140 (2008).
21. Y.-T. Lau *et al.*, Effects of hyperpolarization-activated cyclic nucleotide-gated (HCN) channel blockers on the proliferation and cell cycle progression of embryonic stem cells. *Pflugers Arch.* **461**, 191–202 (2011).
22. A. Omelyanenko, P. Sekyrova, M. Andäng, ZD7288, a blocker of the HCN channel family, increases doubling time of mouse embryonic stem cells and modulates differentiation outcomes in a context-dependent manner. *Springerplus* **5**, 41 (2016).
23. H. Johard *et al.*, HCN channel activity balances quiescence and proliferation in neural stem cells and is a selective target for neuroprotection during cancer treatment. *Mol. Cancer Res.* **18**, 1522–1533 (2020).
24. M. Biel, C. Wahl-Schott, S. Michalakis, X. Zong, Hyperpolarization-activated cation channels: From genes to function. *Physiol. Rev.* **89**, 847–885 (2009).
25. H. J. Kang *et al.*, Spatio-temporal transcriptome of the human brain. *Nature* **478**, 483–489 (2011).
26. M. Florio *et al.*, Human-specific gene ARHGAP11B promotes basal progenitor amplification and neocortex expansion. *Science* **347**, 1465–1470 (2015).
27. G. La Manno *et al.*, Molecular architecture of the developing mouse brain. *Nature* **596**, 92–96, 10.1038/s41586-021-03775-x (2021).
28. A. Ludwig *et al.*, Absence epilepsy and sinus dysrhythmia in mice lacking the pacemaker channel HCN2. *EMBO J.* **22**, 216–224 (2003).
29. M. F. Nolan *et al.*, The hyperpolarization-activated HCN1 channel is important for motor learning and neuronal integration by cerebellar Purkinje cells. *Cell* **115**, 551–564 (2003).
30. J. Stieber *et al.*, The hyperpolarization-activated channel HCN4 is required for the generation of pacemaker action potentials in the embryonic heart. *Proc. Natl. Acad. Sci. U.S.A.* **100**, 15235–15240 (2003).
31. S. Fenske *et al.*, HCN3 contributes to the ventricular action potential waveform in the murine heart. *Circ. Res.* **109**, 1015–1023 (2011).
32. P. Mesirca *et al.*, Cardiac arrhythmia induced by genetic silencing of 'funny' (f) channels is rescued by GIRK4 inactivation. *Nat. Commun.* **5**, 4664 (2014).
33. S. L. Marguet *et al.*, Treatment during a vulnerable developmental period rescues a genetic epilepsy. *Nat. Med.* **21**, 1436–1444 (2015).
34. H. C. Peters, H. Hu, O. Pongs, J. F. Storm, D. Isbrandt, Conditional transgenic suppression of M channels in mouse brain reveals functions in neuronal excitability, resonance and behavior. *Nat. Neurosci.* **8**, 51–60 (2005).
35. J. A. Gorski *et al.*, Cortical excitatory neurons and glia, but not GABAergic neurons, are produced in the Emx1-expressing lineage. *J. Neurosci.* **22**, 6309–6314 (2002).
36. J. Alig *et al.*, Control of heart rate by cAMP sensitivity of HCN channels. *Proc. Natl. Acad. Sci. U.S.A.* **106**, 12189–12194 (2009).
37. S.-X. Wu *et al.*, Pyramidal neurons of upper cortical layers generated by NEX-positive progenitor cells in the subventricular zone. *Proc. Natl. Acad. Sci. U.S.A.* **102**, 17172–17177 (2005).
38. S. Goebbels *et al.*, Genetic targeting of principal neurons in neocortex and hippocampus of NEX-Cre mice. *Genesis* **44**, 611–621 (2006).
39. A. Greco, M. Ittmann, C. Basilico, Molecular cloning of a gene that is necessary for G1 progression in mammalian cells. *Proc. Natl. Acad. Sci. U.S.A.* **84**, 1565–1569 (1987).
40. E. K. Ruzzo *et al.*, Deficiency of asparagine synthetase causes congenital microcephaly and a progressive form of encephalopathy. *Neuron* **80**, 429–441 (2013).
41. I. Y. Hwang *et al.*, Psat1-dependent fluctuations in α-ketoglutarate affect the timing of ESC differentiation. *Cell Metab.* **24**, 494–501 (2016).
42. S. Laguesse *et al.*, A dynamic unfolded protein response contributes to the control of cortical neurogenesis. *Dev. Cell* **35**, 553–567 (2015).

43. J. L. Sánchez-Alonso, J. V. Halliwell, A. Colino, ZD 7288 inhibits T-type calcium current in rat hippocampal pyramidal cells. *Neurosci. Lett.* **439**, 275–280 (2008).
44. R. Felix *et al*., ZD7288 inhibits low-threshold Ca(2+) channel activity and regulates sperm function. *Biochem. Biophys. Res. Commun.* **311**, 187–192 (2003).
45. X. Wu *et al*., Is ZD7288 a selective blocker of hyperpolarization-activated cyclic nucleotide-gated channel currents? *Channels (Austin)* **6**, 438–442 (2012).
46. J. Cai *et al*., Membrane properties of rat embryonic multipotent neural stem cells. *J. Neurochem.* **88**, 212–226 (2004).
47. M. D'Ascenzo *et al*., Role of L-type Ca2+ channels in neural stem/progenitor cell differentiation. *Eur. J. Neurosci.* **23**, 935–944 (2006).
48. G. Lepski, C. E. Jannes, G. Nikkhah, J. Bischofberger, cAMP promotes the differentiation of neural progenitor cells in vitro via modulation of voltage-gated calcium channels. *Front. Cell. Neurosci.* **7**, 155 (2013).
49. A. B. Toth, A. K. Shum, M. Prakriya, Regulation of neurogenesis by calcium signaling. *Cell Calcium* **59**, 124–134 (2016).
50. D. R. Piper, T. Mujtaba, M. S. Rao, M. T. Lucero, Immunocytochemical and physiological characterization of a population of cultured human neural precursors. *J. Neurophysiol.* **84**, 534–548 (2000).
51. H. L. P. Bahrey, W. J. Moody, Voltage-gated currents, dye and electrical coupling in the embryonic mouse neocortex. *Cereb. Cortex* **13**, 239–251 (2003).
52. T. Li, L. Jiang, H. Chen, X. Zhang, Characterization of excitability and voltage-gated ion channels of neural progenitor cells in rat hippocampus. *J. Mol. Neurosci.* **35**, 289–295 (2008).
53. C. G. Lim, S.-S. Kim, H. Suh-Kim, Y.-D. Lee, S. C. Ahn, Characterization of ionic currents in human neural stem cells. *Korean J. Physiol. Pharmacol.* **12**, 131–135 (2008).
54. S. Mirsadeghi *et al*., Development of membrane ion channels during neural differentiation from human embryonic stem cells. *Biochem. Biophys. Res. Commun.* **491**, 166–172 (2017).
55. E. C. Baker *et al*., Functional characterization of Cnidarian HCN channels points to an early evolution of Ih. *PLoS One* **10**, e0142730 (2015).
56. K. Wang *et al*., Electrophysiological properties of pluripotent human and mouse embryonic stem cells. *Stem Cells* **23**, 1526–1534 (2005).
57. L. Linta *et al*., Microarray-based comparisons of ion channel expression patterns: Human keratinocytes to reprogrammed hiPSCs to differentiated neuronal and cardiac progeny. *Stem Cells Int.* **2013**, 784629 (2013).
58. K. Platzer *et al*., *GRIN2B* encephalopathy: Novel findings on phenotype, variant clustering, functional consequences and treatment aspects. *J. Med. Genet.* **54**, 460–470 (2017).
59. A. E. Fry *et al*., De novo mutations in GRIN1 cause extensive bilateral polymicrogyria. *Brain* **141**, 698–712 (2018).
60. R. S. Smith *et al*., Sodium channel SCN3A ($Na_V1.3$) regulation of human cerebral cortical folding and oral motor development. *Neuron* **99**, 905–913.e7 (2018).
61. T. N. Behar *et al*., Glutamate acting at NMDA receptors stimulates embryonic cortical neuronal migration. *J. Neurosci.* **19**, 4449–4461 (1999).
62. P. Reiprich, W. Kilb, H. J. Luhmann, Neonatal NMDA receptor blockade disturbs neuronal migration in rat somatosensory cortex in vivo. *Cereb. Cortex* **15**, 349–358 (2005).
63. Y.-M. Sun *et al*., Distinct profiles of REST interactions with its target genes at different stages of neuronal development. *Mol. Biol. Cell* **16**, 5630–5638 (2005).
64. N. Ballas, C. Grunseich, D. D. Lu, J. C. Speh, G. Mandel, REST and its corepressors mediate plasticity of neuronal gene chromatin throughout neurogenesis. *Cell* **121**, 645–657 (2005).
65. Y. J. Yang *et al*., Microcephaly gene links trithorax and REST/NRSF to control neural stem cell proliferation and differentiation. *Cell* **151**, 1097–1112 (2012).
66. S. McClelland *et al*., The transcription factor NRSF contributes to epileptogenesis by selective repression of a subset of target genes. *eLife* **3**, e01267 (2014).
67. E. L. Jackson *et al*., Analysis of lung tumor initiation and progression using conditional expression of oncogenic K-ras. *Genes Dev.* **15**, 3243–3248 (2001).
68. S. Srinivas *et al*., Cre reporter strains produced by targeted insertion of EYFP and ECFP into the ROSA26 locus. *BMC Dev. Biol.* **1**, 4 (2001).
69. M. Mayford *et al*., Control of memory formation through regulated expression of a CaMKII transgene. *Science* **274**, 1678–1683 (1996).
70. G. Paxinos *et al*., "P0 brain sections" in *Atlas of the Developing Mouse Brain at E17.5, P0 and P6* (Academic Press, ed. 1, 2007).
71. B. Schmalbach *et al*., Age-dependent loss of parvalbumin-expressing hippocampal interneurons in mice deficient in CHL1, a mental retardation and schizophrenia susceptibility gene. *J. Neurochem.* **135**, 830–844 (2015).
72. A. Butler, P. Hoffman, P. Smibert, E. Papalexi, R. Satija, Integrating single-cell transcriptomic data across different conditions, technologies, and species. *Nat. Biotechnol.* **36**, 411–420 (2018).
73. G. Yu, L.-G. Wang, Y. Han, Q.-Y. He, clusterProfiler: An R package for comparing biological themes among gene clusters. *OMICS* **16**, 284–287 (2012).
74. A. Alexa, J. Rahnenfuhrer, Enrichment Analysis for Gene Ontology. R package version 2.30.0 (2016). https://bioconductor.org/packages/release/bioc/html/topGO.html. Accessed 7 November 2019.
75. M. A. Rueger *et al*., Noninvasive imaging of endogenous neural stem cell mobilization in vivo using positron emission tomography. *J. Neurosci.* **30**, 6454–6460 (2010).
76. H. Neuhoff, A. Neu, B. Liss, J. Roeper, I(h) channels contribute to the different functional properties of identified dopaminergic subpopulations in the midbrain. *J. Neurosci.* **22**, 1290–1302 (2002).